Nanoscale Advances

ROYAL SOCIETY OF CHEMISTRY

PAPER

View Article Online
View Journal | View Issue

Cite this: *Nanoscale Adv.*, 2023, **5**, 2804

Te-induced fabrication of $Pt_3PdTe_{0.2}$ alloy nanocages by the self-diffusion of Pd atoms with unique MOR electrocatalytic performance†

Yuhe Shi,‡[a] Ling Zhang, ‡*[a] Huiwen Zhou,[a] Ruanshan Liu, [a] Shichen Nie,[b] Guojie Ye,[c] Fengxia Wu,[de] Wenxin Niu, *[de] Jing Long Han*[fg] and Ai Jie Wang[fg]

The key to the application of direct methanol fuel cells is to improve the activity and durability of Pt-based catalysts. Based on the upshift of the d-band centre and exposure to more Pt active sites, $Pt_3PdTe_{0.2}$ catalysts with significantly enhanced electrocatalytic performance for the methanol oxidation reaction (MOR) were designed in this study. A series of different Pt_3PdTe_x ($x = 0.2$, 0.35, and 0.4) alloy nanocages with hollow and hierarchical structures were synthesized using cubic Pd nanoparticles as sacrificial templates and $PtCl_6^{2-}$ and TeO_3^{2-} metal precursors as oxidative etching agents. The Pd nanocubes were oxidized into an ionic complex, which was further co-reduced with Pt and Te precursors by reducing agents to form the hollow Pt_3PdTe_x alloy nanocages with a face-centred cubic lattice. The sizes of the nanocages were around 30–40 nm, which were larger than the Pd templates (18 nm) and the thicknesses of the walls were 7–9 nm. The $Pt_3PdTe_{0.2}$ alloy nanocages exhibited the highest catalytic activities and stabilities toward the MOR after electrochemical activation in sulfuric acid solution. CO-stripping tests suggested the enhanced CO-tolerant ability due to the doping of Te. The specific activity of $Pt_3PdTe_{0.2}$ for the MOR reached 2.71 mA cm^{-2} in acidic conditions, which was higher than those of Pd@Pt core–shell and $PtPd_{1.5}$ alloy nanoparticles and commercial Pt/C. A DMFC with $Pt_3PdTe_{0.2}$ as the anodic catalyst output a higher power density by 2.6 times than that of commercial Pt/C, demonstrating its practicable application in clean energy conversions. Density functional theory (DFT) confirmed that the alloyed Te atoms altered the electron distributions of $Pt_3PdTe_{0.2}$, which could lower the Gibbs free energy of the rate-determining methanol dehydrogenation step and greatly improve the MOR catalytic activity and durability.

Received 28th August 2022
Accepted 5th April 2023

DOI: 10.1039/d2na00576j

rsc.li/nanoscale-advances

1. Introduction

Direct methanol fuel cells (DMFCs) are considered high-profile renewable and clean energy conversion devices that could help solve the energy and environmental crises thanks to their high conversion efficiency, large safety factor, non-pollution emission, and durable power generation.[1–5] Because of the slow reaction kinetics of the anodic methanol oxidation reaction (MOR), developing efficient anodic electrocatalysts for the MOR is the key to improving the performances of DMFCs.[6] Pt is recognized as a highly efficient electrocatalyst toward the MOR due to its good performance, but the activity sites of Pt can typically get occupied by the CO* intermediates during the catalytic process, leading to a decline in its surface activity or catalytic activity.[7–10] On the other hand, the high price of Pt limits the commercial applications of DMFCs. Therefore, strategies to improve the catalytic activity and CO* anti-poisoning ability of Pt to reduce the usage are urgently needed. Various studies have shown that the MOR catalytic performance of Pt catalysts can be significantly improved by alloying a second or third foreign metal and non-metal elements (*e.g.*, Au, Pd, Rh, Ni, Co, Cu, Sn, Te, P, N) and through adopting unique structures.[11–26]

The use of special defective structures and alloying of oxophilic atoms (Rh, Ir, Pt, Cu, Te, *etc.*) can dramatically weaken the CO* intermediates from methanol and enhance the OH* adsorptions from water molecules, thus benefiting the

[a]*School of Science, Harbin Institute of Technology, Shenzhen, 518055, China. E-mail: zhangling2018@hit.edu.cn*

[b]*Shandong Hynar Water Environmental Protection Co., Ltd, Heze, 274400, China*

[c]*Hynar Water Group Co., Ltd, Shenzhen, 518052, China*

[d]*State Key Laboratory of Electroanalytical Chemistry, Changchun Institute of Applied Chemistry, Chinese Academy of Sciences, Changchun, 130022, China. E-mail: niuwx@ciac.ac.cn*

[e]*University of Science and Technology of China, Anhui, 230026, China*

[f]*School of Civil and Environmental Engineering, Harbin Institute of Technology, Shenzhen, 518055, China. E-mail: hanjinglong@yeah.net*

[g]*State Key Laboratory of Urban Water Resource and Environment (Shenzhen), Harbin Institute of Technology, Shenzhen, 518055, China*

† Electronic supplementary information (ESI) available: ICP-OES, TEM, DFT data. See DOI: https://doi.org/10.1039/d2na00576j

‡ These authors contributed equally.

oxidation of methanol into CO_2 and avoiding the poisoning of the Pt active sites.[8,11,13,15,27,28] Meanwhile, the d-centre of Pt can be lowered dramatically and the electronic environment optimized with synergistic effects achieved to further improve the catalytic activities and durability of Pt-based catalysts. For example, disordered Pt_3Sn nanocubes,[8] Cu-incorporated PtBi intermetallic nanofiber bundles,[11] defect-rich PtTeCo nanorods,[13] ultrathin PtNiRh nanowires,[15] and Pt–Ni–P mesoporous nanocages with high surface porosity[18] have been synthesized with the typical solvothermal, hydrothermal, and template-sacrifice methods. All these nanocomposites showed much higher electrocatalytic activities and stabilities towards the MOR than those of commercial Pt/C catalysts due to the optimized electronic structures of the Pt sites from the strain and ligand effects of the defective and alloying structures.[18]

Nanocages are considered among the most highly efficient structures and can greatly improve the utilization of the costly noble metal catalysts.[18,19,29] Their ultrathin walls, rich surface porosities, and hollow structures endow nanocages with large surface areas, short charge-transport distances, and fast mass-transport processes. Up to now, Pt-based nanocage catalysts have been achieved by template-sacrifice,[18] acidic etchings,[19,29,30] and galvanic replacement reactions.[31,32] Te nanowires and nanosheets are usually as the templates to obtain Pt- and Pd-based alloy hollow and porous nanostructures or ultrathin nanowires through galvanic replacement reactions.[21,33,34] The final PtTe relevant alloy nanostructures exhibited unique electrocatalytic activities towards the MOR, hydrogen evolution reaction (HER), and oxygen reduction reaction (OER). Moreover, it was demonstrated by density functional theory (DFT) calculations that Te could help to activate OH^- and promote Pt to more easily oxidize the CO* intermediates to CO_2 during the formic acid electrooxidation.[35] Thus, developing Te-alloyed Pt-based electrocatalysts with high surface areas and porosity would greatly promote their MOR electrocatalytic activities and durability.

In this regard, we developed a new strategy to obtain Pt_3PdTe_x ($x = 0.2$, 0.35, and 0.4) trimetallic cubic alloy nanocages with porous and hollow structures by the self-diffusion of Pd atoms. As a test, H_2PtCl_6 and Na_2TeO_3 were reduced by ascorbic acid in the presence of the as-prepared 18 nm Pd cubes and cetyltrimethylammonium bromide (CTAB) at 60 °C. The Pd cubes were oxidatively etched in this condition and face-centred cubic (fcc) Pt_3PdTe_x alloy nanocages sized around 30–40 nm were automatically formed. The thicknesses of the nanocages were in the range of 7–9 nm, depending on the components of Te in the alloy nanocages. The reported synthetic method avoids the traditional need for harsh reaction conditions, *e.g.*, high pressure, high temperature, and toxic reagents.[10,33,36] Thanks to the alloy, and porous and hollow structures, the obtained $Pt_3PdTe_{0.2}$ nanocages showed much higher MOR electrocatalytic activities, durability, and anti-fouling ability than those of Pd@Pt, $PtPd_{1.5}$, and the commercial Pt/C. DFT calculations demonstrated that the rate-limiting step of the $Pt_3PdTe_{0.2}$ nanocages in the MOR process was breaking the C–H bond of methanol to form $*CH_2OH$, for which the reaction free energy was much lower than those for Pt and Pt_3Pd. The d-band centre of $Pt_3PdTe_{0.2}$ was the closest to the Fermi level, further demonstrating the good durability of the $Pt_3PdTe_{0.2}$ catalysts.

2. Experimental section

2.1 Reagents

$H_2PtCl_6 \cdot 6H_2O$ (Reagent grade), KOH (BC grade, ≥85%), and $PdCl_2$ (BC grade) were purchased from Sangon Biotech (Shanghai) Co., Ltd. Cetyltrimethylammonium bromide (≥98%) and L-ascorbic acid (Reagent grade, ≥98%) were obtained from Sigma-Aldrich. Na_2TeO_3 (Reagent grade, ≥98%) and methanol (≥99%) were purchased from Adamas Co., Ltd. Sulfuric acid (Reagent grade, 95–98%) and hydrochloric acid (Ultrapure, 36–38%) were obtained from Tansole Co., Ltd (Shanghai). Commercial Pt/C (Pt loading, 20 wt%) was obtained from Macklin. All the chemicals were used without further purification. Ultrapure water (18.2 MΩ cm) was used throughout the experiments. The H_2PdCl_4 mother solution (10 mM) was prepared by dissolving 0.1773 g of $PdCl_2$ powders in 10 mL of 0.2 M HCl aqueous solution and further diluting to 100 mL with ultrapure water.

2.2 Instruments

Scanning electron microscopy (SEM) characterizations were performed on an Hitachi SU8010 field-emission microscope operated at 5 kV. Transmission electron microscopy (TEM) characterizations, high-resolution TEM (HR-TEM), high-angle annular dark-field scanning transmission electron microscopy (HAADF-STEM), energy dispersive spectrometry (EDS), and elemental mapping analyses were performed on a JEOL JEM-3200FS microscope at 300 kV. X-Ray diffraction (XRD) patterns were collected on a Rigaku SmartLab system (Cu Kα radiation). Inductively coupled plasma-optical emission spectrometry (ICP-OES) data for the weight concentrations of the metal elements of the as-produced solutions were obtained on a Spectro Arcos II MV instrument. X-Ray photoelectron spectroscopy (XPS) measurements were conducted on an ESCALAB-MKII spectrometer (VG Co., United Kingdom) with Al Kα X-ray radiation as the X-ray source for excitation.

2.3 Synthesis of the cubic Pd templates

Pd cubes with sizes of 17.8 ± 2.0 nm were synthesized according to a previous method.[37] Briefly, 0.5 mL of 10 mM H_2PdCl_4 solution was added to 10 mL of 12.5 mM CTAB solution under stirring and refluxing at 95 °C in an oil bath. After 5 min, 80 μL of 100 mM ascorbic acid solution was added quickly. The reaction proceeded for 30 min. Finally, the solution of Pd cubes was kept at 30 °C for future use.

2.4 Synthesis of Pt_3PdTe_x porous alloy nanocages

In a typical synthesis, 100 μL of 1 M HCl solution, 100 μL of 10 mM H_2PtCl_6, and 0.72 mL of Pd cubes solution were added into 8 mL of 50 mM CTAB solution in multiple vessels and parallelly kept in a water bath at 60 °C. After shaking up and standing for 5 min, 20, 40, and 100 μL of 10 mM Na_2TeO_3 solution was added into each vessel to produce $Pt_3PdTe_{0.2}$,

$Pt_3PdTe_{0.35}$, and $Pt_3PdTe_{0.4}$ porous alloy nanocages, respectively. Then, 0.3 mL of 0.1 M ascorbic acid solution was added, and the solutions were shaken up gently and allowed to stand for reacting. After 6 h, the as-products were collected and washed with hydro–alcohol (1 : 1) mixture solution by centrifugations (12 000 rpm, 5 min) five times. The final products were dispersed in 200 μL hydro–alcohol (1 : 1) solution for the electrocatalytic experiments, respectively.

Pd@Pt core–shell nanoparticles were produced by following the similar steps as for Pt_3PdTe_x, except that Na_2TeO_3 precursor solutions were not introduced. $PtPd_{1.5}$ alloy nanoparticles were also produced by following similar steps as for Pt_3PdTex except that 100 μL of 10 mM H_2PdCl_4 aliquot was added to replace the cubic Pd templates and the Na_2TeO_3 precursors were not added. The weights of Pt and Pd elements in the as-produced dispersion solutions were measured by ICP-OES.

2.5 Electrochemical measurements

The electrochemical measurements were conducted on a CHI 760E electrochemical workstation (Shanghai Chenhua Instrument Co., Ltd, China). Briefly, in a three-electrode system, Ag/AgCl (saturated KCl) was used as the reference electrode, Pt piece as the counter electrode, and the catalyst-coated glassy carbon electrode (GCE) with a diameter of 4 mm was used as the working electrode. For preparations of the working electrodes, the GCE was first polished with 0.3 and 0.05 μm Al_2O_3 slurries and sonicated in water, respectively. After drying, 12 μL of the Pt_3PdTe_x, Pd@Pt, and PtPd, and Pt/C catalysts inks were cast onto the GCE and room-dried for the MOR and CO-stripping experiments, respectively.

The electrochemically active surface area (ECSA, cm^2) was determined by integrating the monolayer hydrogen adsorption peaks at 0.05–0.35 V *vs.* RHE in the cyclic voltammograms (CVs) in 0.5 M H_2SO_4 solutions according to eqn (1),[38]

$$\mathrm{ECSA} = \frac{Q}{0.21\ \ (\mathrm{mC\ cm^{-2}})} \tag{1}$$

where Q is the charge for the monolayer hydrogen adsorption on the catalysts surface, mC.

CO-stripping experiments were performed in 0.5 M H_2SO_4. First, the electrocatalyst-modified GCEs were electrochemically activated in 0.5 M H_2SO_4 for 20 cycles by sweeping in the potential range of 0–1.2 V (*vs.* RHE). Second, the electrolytes for CO stripping were bubbled with CO for 15 min. Third, CO adlayers were formed by applying −0.3 V (*vs.* RHE) for 15 min to the electrocatalyst-modified GCEs under a CO atmosphere. Fourth, N_2 was bubbled into the electrolyte for 10 min. Finally, the GCEs were swept in the range of 0–1.2 V (*vs.* RHE) to achieve CO-stripping curves. The relative adsorption amounts of the CO adlayer on the electrocatalysts (p, %) were calculated using eqn (2),

$$p = \frac{S_1 - S_3}{s_3} \tag{2}$$

where S_1 and S_3 represent the charges for monolayer CO adsorbed on the catalysts in the potential range of 0.6–1.2 V *vs.* RHE in segments 1 and 3 of the CVs for CO stripping, mC cm^{-2}.

Toray carbon papers and 1 mg cm^{-2} Pt particles-loaded carbon papers (10 cm × 10 cm × 0.19 mm) were purchased to fabricate DMFC. $Pt_3PdTe_{0.2}$ (x = 0.2, 0.35, and 0.4) and commercial Pt/C were used as anodic catalysts to promote the MOR. The commercial Pt particles-loaded carbon papers were used as cathodes to catalyse the ORR. Briefly, the carbon papers were cut into smaller sizes with a length × width of 1.5 × 1 cm. Next, 80 μL electrocatalysts was cast onto the carbon papers with area of 0.5 × 1 cm, which were room-dried and swept in the range of 0–1.25 V (*vs.* RHE) in 0.5 M H_2SO_4 for 50 cycles to be used as anodes. The length × width of the part immersed into the electrolytes were 0.5 × 1 cm. Also, 0.1 M $HClO_4$ was used as the electrolytes in DMFC, and the anodic and cathodic chambers were separated by a Nafion film. The electrolytes in the cathodic chamber were bubbled with O_2 for 30 min before the tests and the flow was controlled above the liquid surface to maintain an O_2 atmosphere during the tests.

2.6 Computational methods

We employed the plane-wave code Vienna *ab initio* simulation package (VASP) program to perform all the spin-polarized DFT calculations within the generalized gradient approximation (GGA) using the Perdew–Burke–Ernzerhof (PBE) formulation.[39–41] We chose the projected augmented wave (PAW) potentials to describe the ionic cores and took the valence electrons into account by using a plane-wave basis set with a kinetic energy cut-off of 500 eV.[42,43] The valence electron configurations applied in this work were $1s^1$(H), $2s^22p^2$(C), $2s^22p^4$(O), $5s^24d^9$(Pd), $5s^25p^4$(Te), and $6s^15d^9$(Pt), respectively. Partial occupancies of the Kohn–Sham orbitals were allowed using the Gaussian smearing method and a width of 0.02 eV. The electronic energy was considered self-consistent when the energy change was smaller than 10^{-6} eV.

The equilibrium lattice constants of the [Pt] unit cell were optimized using an 8 × 8 × 8 Monkhorst–Pack k-point grid for Brillouin zone sampling as $a = b = c = 3.91643$ Å. These lattice constants were used to build the Pt(111) surface slab with 4 atomic layers, which contained 64 Pt atoms. The surfaces mentioned above were chosen since these surfaces were exposed on the surface of the materials, as confirmed by the HRTEM studies. This slab was separated by a 15 Å vacuum layer in the z direction between the slab and its periodic images. During structural optimization of all the surface models, a 3 × 3 × 1 gamma-point centred k-point grid for the Brillouin zone was used. Also, all the atomic layers were allowed to fully relax. In addition, the Pd and Te atoms were located in the Pt structure to consider the effect of the Pd and Te.

The Gibbs free energy (G, eV) at 298 K was calculated by eqn (3),

$$G = H - T\Delta S = E_{\mathrm{DFT}} + E_{\mathrm{ZPE}} - TS \tag{3}$$

where H is the enthalpy, eV; S the entropy, eV; T the temperature, K; E_{DFT} the total energy from the DFT calculations, eV; and E_{ZPE} the zero-point energy, eV.

3. Results and discussion

3.1 Synthesis and structural characterizations of the porous Pt_3PdTe_x nanocages

In a typical synthesis, Pt_3PdTe_x (x = 0.2, 0.35, and 0.4) nanocages having a hollow structure were synthesized with Pd cubes (17.8 ± 2.0 nm, Fig. S1†) as sacrificial templates, H_2PtCl_6 and Na_2TeO_3 as chemical corrosion agents, and CTAB as a capping agent (Scheme 1). Both H_2PtCl_6 and Na_2TeO_3 etched Pd cubes into $PdBr_4^{2-}$ complex anions. Meanwhile, all the $PtCl_6^{2-}$, TeO_3^{2-}, and $PdBr_4^{2-}$ complexes were reduced by ascorbic acid, so that Pt_3PdTe_x alloy nanoparticles with hollow structures and porous surfaces were produced. The as-produced compounds all exhibited cubic shapes the same as the Pd templates (Fig. 1a and S2–S4†). The atomic ratios of Pt and Pd and Te elements in the products were calculated from the ICP-OES results (Table S1†). The sizes of the $Pt_3PdTe_{0.2}$ nanocages were measured to be 29.2 ± 4.7 nm and the thickness of the nanocages was estimated to be 7.3 nm (Fig. 1b). Apparently hollow structures were observed from the TEM analysis (Fig. 1) From the local amplified area, the lattice spacing of the $Pt_3PdTe_{0.2}$ nanocages was measured to be 0.209 nm, which was close to those of the (100) facets of the face-centred cubic (fcc) Pt and Pd (Fig. 1c and d). The hollow structures of $Pt_3PdTe_{0.2}$ were also confirmed by EDS and line-scanning elemental analysis (Fig. 1e and f). There were little elemental signals for Pt, Pd, and Te in the middle parts in the EDS images, and the signals in the middle were smaller than those at the edges of $Pt_3PdTe_{0.2}$ in the line-scanning profiles.

The content of elemental Te in the as-produced compounds was affected by the amount of Na_2TeO_3 introduced into the growth solution. With the volume of 10 mM Na_2TeO_3 aliquots added increasing from 20 μL to 40 and 100 μL, the ratio of Te in the as-produced compounds increased. The as-produced compounds were $Pt_3PdTe_{0.35}$ and $Pt_3PdTe_{0.4}$, respectively (Fig. S3 and S4†). The same hollow structures were formed. The sizes of the nanocages were 42.5 ± 8.6 and 28.4 ± 4.5 nm, and the thicknesses were 8.5 and 6.7 nm for $Pt_3PdTe_{0.35}$ and $Pt_3PdTe_{0.4}$, respectively. The alloying of low contents of Te (4.1–6.4 wt%, Table S1†) did not alter the crystal structures or lattice

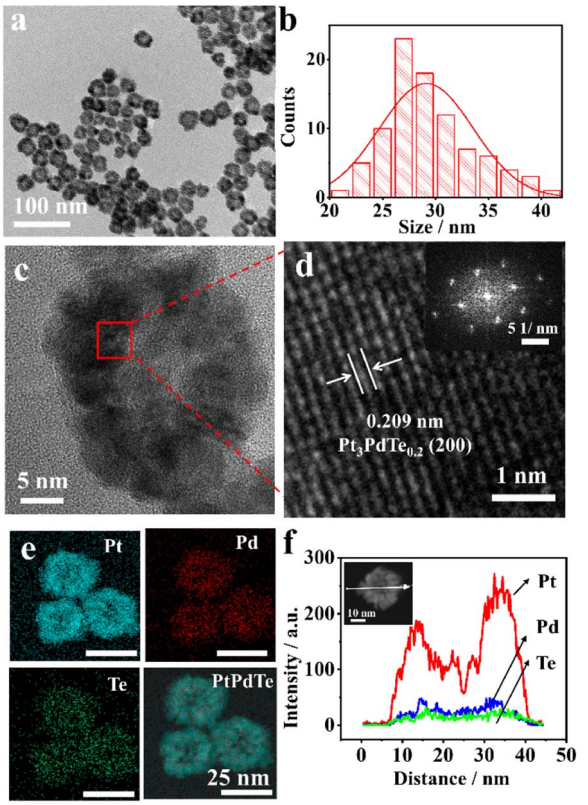

Fig. 1 TEM image (a) and size distribution (b), HRTEM images (c and d), and EDS elemental mappings (e) of $Pt_3PdTe_{0.2}$ nanocages. Inset of (d), corresponding FFT (fast Fourier transform) pattern. (f) Elemental line-scanning profile across the white arrow of an individual $Pt_3PdTe_{0.2}$ nanocage (inset).

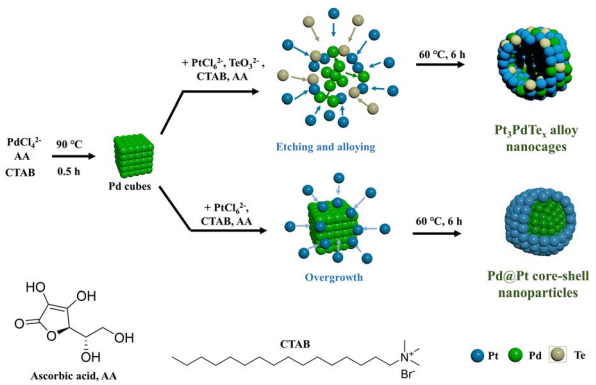

Scheme 1 Synthetic process diagram of Pt_3PdTe_x alloy nanocages and Pd@Pt core–shell nanoparticles.

spacings of the alloy nanocages apparently. All three kinds of Pt_3PdTe_x nanocages belonged to fcc noble metal crystal structures. The lattice spacings of $Pt_3PdTe_{0.35}$ and $Pt_3PdTe_{0.4}$ were measured to be 0.205 nm, and could be fitted to the (100) facets of fcc Pt and Pd (Fig. S3e and S4e†).

Thanks to the presence of TeO_3^{2-} ions in the growth solutions, Pt_3PdTe_x alloy structures could be formed. Without TeO_3^{2-}, the products were cubic core–shell nanoparticles composed of cubic Pd cores and Pt shells (Fig. S5†). The Pd cubes could not be etched in the absence of TeO_3^{2-}. The lattice spacing of the Pt shell was measured to be 0.226 nm, which could be fitted to Pt(111) (Fig. S5d†). Cubic Pd centres were clearly exhibited in the EDS images (Fig. S5e†). Pt shells were formed around Pd, exhibiting strong EDS signals in the outer part. Also, the Pd signals were stronger than those of Pt in the middle part of the nanoparticles in the line-scanning profiles, further confirming the core–shell structures (Fig. S5f†). The sizes of the Pd@Pt core–shell nanoparticles were 36.8 ± 6.8 nm, while the thickness of the Pt shells was estimated to be 9.5 nm according to the TEM results. These results indicated that TeO_3^{2-} was important to induce the etching process of the Pd cubes and the formations of Pt_3PdTe_x alloy nanoparticles with hollow structures. This may be due to the oxidative properties of Te, which probably vulcanized Pd and Pt somehow, resulting in the etching process of the Pd cubes.

The XRD characterizations further reflected the crystalline structures of Pt_3PdTe_x alloy nanocages and Pd@Pt core–shell nanoparticles (Fig. 2). Typical peaks for the (111), (200), (220), and (311) facets of fcc noble metal nanocrystals were clearly exhibited (Pt pdf #04-0802, Pd JCPDS no. 05-0681).[44,45] The incorporation of Te into PtPd alloy crystals induced small negative offsets in the peak positions due to the lower diffraction angles of Te with a trigonal phase (JCPDS no. 85-0554) than those of Pt and Pd.[46] This indicated that Pt_3PdTe_x alloyed nanostructures were formed successfully by the self-diffusion of Pd atoms.

To analyze the structures and valences of the surface chemical elements of the catalysts, XPS characterizations were conducted (Fig. 3). The main peaks at 73.9 and 70.5 eV could be fitted to Pt $4f_{5/2}$ and Pt $4f_{7/2}$ energy levels, respectively (Fig. 3a). Interestingly, shoulder peaks at 74.9 and 71.6 eV were found for all the Pt_3PdTe_x alloy and Pd@Pt core–shell nanoparticles, which were attributed to Pt(II) $4f_{5/2}$ and Pt(II) $4f_{7/2}$ valence states, respectively. Such XPS peaks for the Pt(II) valence states were also reportedly observed for PtPdCu particles previously, which may be due to the formation of micro PtO and $Pt(OH)_2$.[22] Compared with Pd@Pt core–shell nanoparticles, the binding energies of Pt 4f for the three kinds of Pt_3PdTe_x alloy nanocages were all shifted positively, for which $Pt_3PdTe_{0.2}$ exhibited the greatest positive change (about 0.25 eV). Additionally, trace charge transfer occurred when Te was incorporated into the PtPd bimetallic alloy nanostructures, thus leading to the enhanced peak area ratios of Pt(II)/Pt(0) and the transitions from Pt(0) to Pt(II).[47] Regarding the XPS of the surface Te composites of Pt_3PdTe_x (Fig. 3b), the Te(IV) valence states predominated. Also, the main peaks at 586.3 and 575.9 eV could be fitted to Te(IV) $3d_{3/2}$ and $3d_{5/2}$ energy levels, while the shoulder peaks at 583.6 and 573.1 eV belonged to Te(0) $3d_{5/2}$ and $3d_{5/2}$, respectively.[13] The observation of peaks for Pd(0) $3d_{3/2}$ and $3d_{5/2}$ clearly indicated Pt_3PdTe_x alloy nanocages, while there were no XPS signals suggesting Pd@Pt core–shell nanoparticles. The XPS results suggested the vulcanizations of Pt and Pd by Te and the presence of tellurides in the noble metal-based alloy nanocrystals.

3.2 Reconstitutions of Pt_3PdTe_x by electrochemical activation

Before the electrocatalytic studies for the MOR, Pt_xPdTe_y alloy nanocages, Pd@Pt core–shell, $PtPd_{1.5}$ alloy (55.4 ± 9.6 nm,

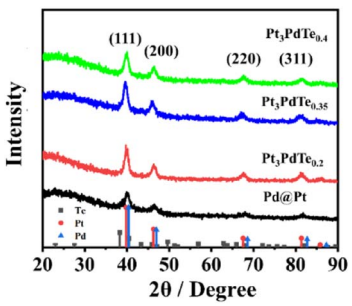

Fig. 2 XRD patterns of Pt_3PdTe_x nanocages and Pd@Pt core–shell nanoparticles.

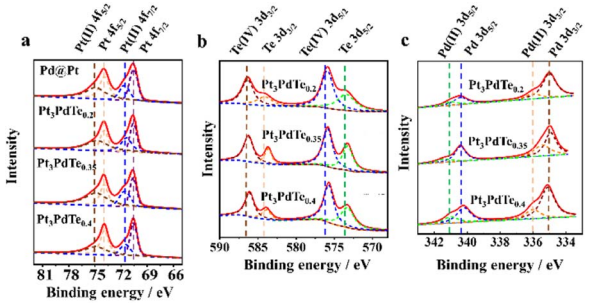

Fig. 3 XPS spectra of Pt (a), Te (b), and Pd (c) elements of Pt_3PdTe_x-nanocages and Pd@Pt core–shell nanoparticles.

Fig. S6†), and commercial Pt/C catalysts were electrochemically activated in 0.5 M H_2SO_4 solution to obtain clean surfaces (Fig. 4a and S7†). The hydrogen adsorption/desorption peaks located in 0.05–0.35 V *vs.* RHE for the Pt_3PdTe_x alloy nanocages started to form in the second CV cycle, which became larger with activation and became stable up to the 50th CV cycle (Fig. S7a–c†). Regarding Pd@Pt, $PtPd_{1.5}$, and Pt/C, there were obvious hydrogen adsorption/desorption peaks in the first CV cycle, which differed from those in Pt_xPdTe_y (Fig. S7d–f†). This difference may be due to some Te atoms blocking the active sites of Pt, which were then dissolved in the electrolyte solutions

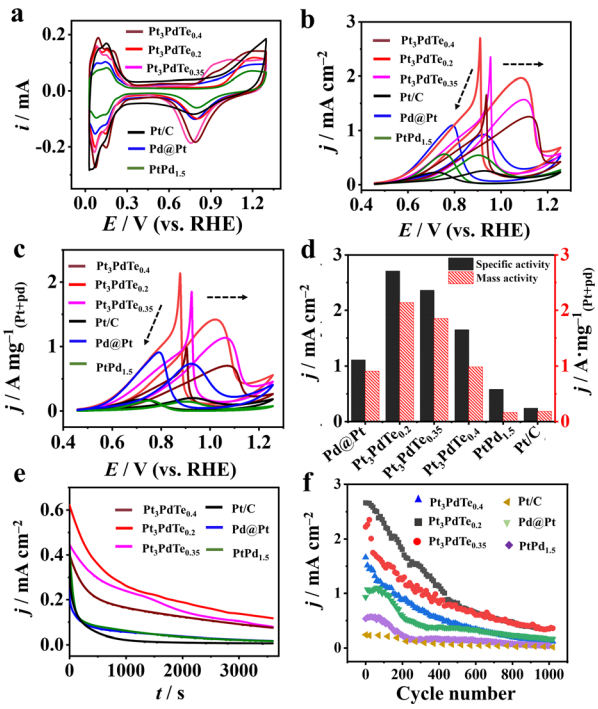

Fig. 4 (a) CVs after 50 cycles of different catalyst-modified GCEs in 0.5 M H_2SO_4 in an Ar atmosphere. Scanning rates, 50 mV s^{-1}. (b and c) Specific activities and mass activity curves of different catalysts towards the electrooxidation of 1 M methanol in 0.1 M $HClO_4$. Scanning rate of 50 mV s^{-1}. (d) Maximum specific activities and mass activities in the backward scans of different catalysts. Durability tests towards the electrooxidation of 1 M methanol by chronoamperometry at 0.76 V for 3600 s (e) and cyclic voltammetry for 1000 cycles (f).

after the electrochemical activation in the acidic medium. TEM-EDS elemental analysis demonstrated that some Te was lost after this process (Table S2†). After the electrochemical activation, Pt_3PdTe_x alloy nanocages were stable and feasible to be applied as electrocatalysts.

3.3 MOR catalytic behaviours

The electrocatalytic performances of Pt_3PdTe_x, Pd@Pt, $PtPd_{1.5}$, and Pt/C catalysts towards the MOR were investigated in 0.1 M $HClO_4$ medium. Stronger specific activities and mass activities of the three kinds of Pt_3PdTe_x alloy nanocages were observed than those for Pd@Pt, $PtPd_{1.5}$, and Pt/C (Fig. 4b and c). The catalytic activity and Pt and Pd utilization efficiencies of $Pt_3PdTe_{0.2}$ were the best. The specific activities of $Pt_3PdTe_{0.2}$, $Pt_3PdTe_{0.35}$, $Pt_3PdTe_{0.4}$, Pd@Pt, $PtPd_{1.5}$, and Pt/C at 0.76 V *vs.* RHE were 2.71, 2.36, 1.65, 1.11, 0.58, and 0.24 mA cm^{-2} in the backward scan, respectively (Fig. 4d and Table S3†), and the mass activities were 2.14, 1.85, 0.98, 0.91, 0.16 and 0.18 A mg_{Pt+Pd}^{-1}, respectively (Fig. 4d and Table S3†). It can be inferred that the alloying of Te into PtPd and the formation of a hollow structure with a porous surface greatly enhanced the electrocatalytic activity towards the MOR. More importantly, Pt_3PdTe_x alloy nanocages had higher ratios of the backward peak currents to the forward peak currents (I_b/I_f), indicating the good anti-poisoning ability towards CO intermediates during the MOR (Table S3†). The CO-stripping experiments indicated the better CO-tolerance properties of the Te-doped Pt nanocages (Fig. 5).

Regarding Pt_3PdTe_x, there were two CO oxidation peaks, and the peaks located around 0.86–0.88 V *vs.* RHE were induced by the presence of Te (Fig. 5a). The relative amounts of adsorbed CO on Pt_3PdTe_x were lower than those of Pd@Pt and Pt/C (eqn (2), Fig. 5b and S8†). Compared to the previous reports, the $Pt_3PdTe_{0.2}$ alloy nanocages showed better specific catalytic activity and mass activity than those of most PtTe-based alloy nanowires/nanotubes and PtPd-based alloy nanowires/dendrites (Table S4†).[10,21,48–51] It was demonstrated that both the alloyed Te composites and hollowed structures of $Pt_3PdTe_{0.2}$ developed in this work were important to improve the MOR catalytic activity.

Moreover, the $Pt_3PdTe_{0.2}$ nanocages exhibited the best durability among the Pt, PtPd, and Pt_3PdTe_x related catalysts. After 3600 s at 0.76 V, the MOR specific activity was the highest and could be maintained at 23% of the initial activity (Fig. 4e and S9a†). After 1000 cycles in 1 M methanol, $Pt_3PdTe_{0.2}$ maintained 14% specific activity and mass activity. These activities were higher than those of Pd@Pt core–shell, $PtPd_{1.5}$ alloy, and commercial Pt/C catalysts by 1.27, 7.67, and 20.94 times, respectively (Fig. 4f and S9b†). The $Pt_3PdTe_{0.2}$ nanocages had stable structures after the durability tests in acidic medium (Table S2†). The mass percentage of Te in $Pt_3PdTe_{0.2}$ was not decreased, and the hollowed nanocage structures were well maintained (Fig. 6). To demonstrate the practicability of the $Pt_3PdTe_{0.2}$ nanocages for producing clean energy, DMFCs were fabricated with $Pt_3PdTe_{0.2}$ as the anodic catalyst. The output voltage for the DMFC with $Pt_3PdTe_{0.2}$ was 0.2 V, which was larger than that of commercial Pt/C by 50 mV. The maximum output power density for $Pt_3PdTe_{0.2}$ were 17.8 μW cm^{-2}, which were higher than those of Pt/C by 2.6 times (Fig. 7).

Furthermore, the stabilities of the DMFCs with $Pt_3PdTe_{0.2}$ catalysts were better than those of Pt/C, whereby the output current densities could be maintained at 80 and 40% in 2 h at 0.1 V, respectively.

3.4 DFT calculations

Based on the experimental data from the structural and compositional analyses, DFT computational models for Pt, Pt_3Pd alloy, and $Pt_3PdTe_{0.2}$ alloy were established, which were used to further elucidate the mechanism of the MOR. We constructed a complete reaction network, including the activation energies and all the optimized structures of the intermediates to investigate the preferred pathway for the process from methanol to CO_2. Gibbs free energy curves of the preferred reaction paths were drawn according to the calculated data (Fig. 8). The interacting atoms of the –OH*-containing intermediates (CH_2OH*, CHOH*, COH*) with sites in the three catalysts were the C atoms, rather than the O atoms for the –O*-containing intermediates (CO*, CH_3O*, CH_2O*, CHO*), as shown in Fig. 9 and S10–S12.† It was found that on the sites of Pt, Pt_3Pd, and $Pt_3PdTe_{0.2}$, methanol was more inclined to break the C–H bonds producing CH_2OH* than the O–H bonds producing CH_3O* first (Fig. 8 and 9). Then, H atoms were removed from the unsaturated C sites of CH_2OH* intermediates one by one. Finally, CO* intermediates were produced and oxidized into CO_2 products (Fig. 10a). The preferred paths were $CH_3OH \rightarrow CH_2OH^* \rightarrow CHOH^* \rightarrow COH^* \rightarrow CO^* \rightarrow CO_2$. The rate-limiting step for the

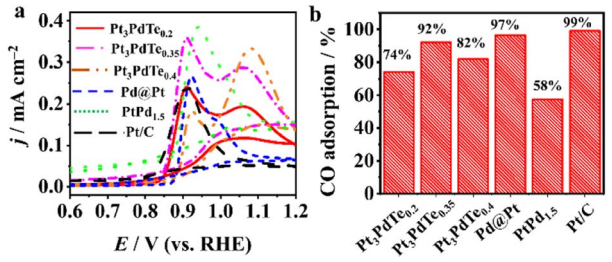

Fig. 5 (a) CO-stripping curves of different electrocatalysts in 0.5 M H_2SO_4. Scanning rate, 50 mV s^{-1}. (b) Relative adsorption amounts of CO on the electrocatalysts calculated by eqn (2).

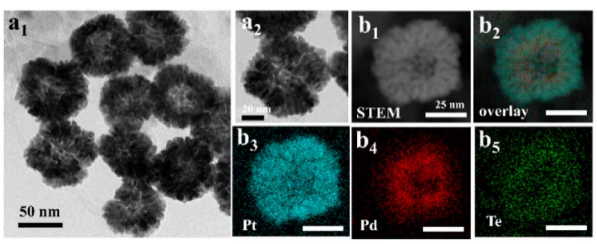

Fig. 6 TEM images (a_1 and a_2), STEM image (b_1), and EDS elemental mapping (b_2–b_5) of $Pt_3PdTe_{0.2}$ catalysts after the durability test in 0.1 M $HClO_4$ towards the MOR.

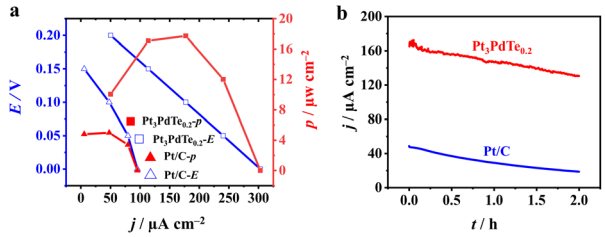

Fig. 7 (a) Output voltage (left axis) and power density (right axis) of fuel cells with $Pt_3PdTe_{0.2}$ and Pt/C catalysts as anodic catalysts. (b) Stability of fuel cells running at 0.1 V *vs.* RHE. Anode, 1 M methanol; cathode, O_2 atmosphere; electrolytes, 0.1 M $HClO_4$.

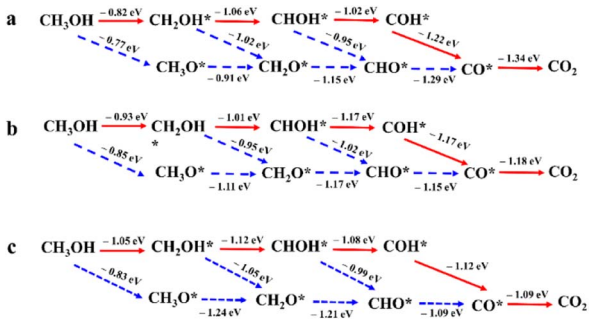

Fig. 8 Reaction networks of the MOR for Pt (a), Pt_3Pd (b), and $Pt_3PdTe_{0.2}$ (c).

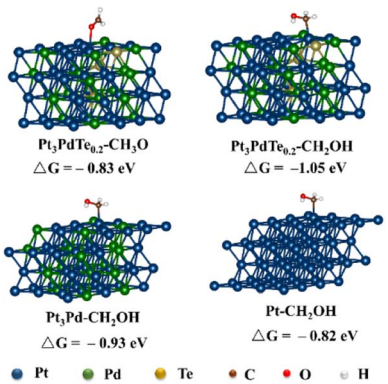

Fig. 9 Configurations of the three kinds of catalysts and Gibbs free energy change diagrams of the first step of the MOR.

three catalysts in the MOR process were all the breaking of the C–H bonds of methanol to generate $*CH_2OH$, for which the energy barriers were significantly higher than those of the other basic steps.

Moreover, the reaction activity of this rate-determination step catalyzed by the $Pt_3PdTe_{0.2}$ alloy (ΔG, −1.05 eV) was calculated to be higher than with the Pt_3Pd alloy (ΔG, −0.93 eV) and Pt (ΔG, −0.82 eV), indicating the excellent performance of the Te-alloyed PtPd in the MOR. In the CO* oxidation process, O* began to form on the surface of catalysts and coupled with CO* to finally produce CO_2.

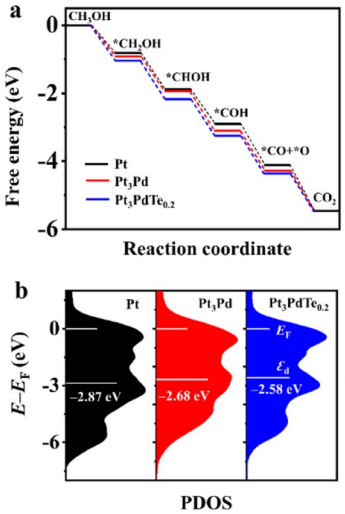

Fig. 10 (a) Gibbs free energy change diagrams of the MOR process on Pt, Pt_3Pd, and $Pt_3PdTe_{0.2}$ (U = 0.624 V). (b) PDOS and ε_d of Pt, Pt_3Pd, and $Pt_3PdTe_{0.2}$, with E_F set to zero.

The partial density of states (PDOS) and d-band centre (ε_d) were calculated to demonstrate the change in the electronic structure for Pt, Pt_3Pd, and $Pt_3PdTe_{0.2}$ (Fig. 10b). The d-band centre of $Pt_3PdTe_{0.2}$ was closer to its Fermi level (E_F) compared with Pt and Pt_3Pd, indicating that when it adsorbs intermediates, less electrons will be filled into the antibonding orbitals.[52] Thus, the intermediates on the $Pt_3PdTe_{0.2}$ catalysts were easier to be oxidized during the MOR, explaining the better activity and durability of $Pt_3PdTe_{0.2}$ than those of Pt and PtPd related catalysts.

4. Conclusion

To summarize, a new method for preparing Pt_3PdTe_x hollow nanocages was proposed. Differing from the previous reports, it employed a Pd nanocubes template instead of Te nanowires template, avoiding the need for harsh synthetic conditions. The obtained $Pt_3PdTe_{0.2}$ nanocages displayed much higher electrocatalytic specific and mass activities and stabilities than those of Pt and PtPd reference electrocatalysts towards the MOR in acidic medium after electrochemical activation. Thanks to the hollow structures and porous surfaces and the alloying effect of oxophilic Te atoms, the $Pt_3PdTe_{0.2}$ alloy nanocages exhibited much better catalytic performance. DFT studies confirmed that the Gibbs free energy of the rate-determining step of the MOR catalyzed by $Pt_3PdTe_{0.2}$ was lowered and the d-band centre of $Pt_3PdTe_{0.2}$ was shifted to E_F, leading to the great catalytic activity and durability. Thus, the study is important to improve the Pt utilization in DMFCs and shows the importance of optimizing the shapes and performance of hollow PtPdTe electrocatalysts.

Author contributions

Yuhe Shi undertook the experiments and processed the data. Yuhe Shi and Ling Zhang conceived the idea and wrote the

original draft. Ling Zhang, Wenxin Niu, Jing Long Han, and Ai Jie Wang supervised and revised the paper. All the authors discussed the result, revised the paper, and approved the final version.

Conflicts of interest

There are no conflicts to declare.

Acknowledgements

This work was kindly supported by the National Natural Science Foundation of China (22004024), Shandong Provincial Key Research and Development Program (2020CXGC011202-001), Shenzhen College Stability Support Plan (GXWD20201230155427003-20200821182144001), and Starting Research Grant for High-Level Personnel Overseas of Shenzhen City (Peacock Plan).

Notes and references

1 E. Antolini, *Appl. Catal., B*, 2018, **237**, 491–503.
2 H. Xu, H. Shang, C. Wang and Y. Du, *Adv. Funct. Mater.*, 2020, **30**, 2000793.
3 W. Li, D. Wang, Y. Zhang, L. Tao, T. Wang, Y. Zou, Y. Wang, R. Chen and S. Wang, *Adv. Mater.*, 2020, **32**, 1907879.
4 X. Yang, Y. Wang, X. Tong and N. Yang, *Adv. Energy Mater.*, 2021, **12**, 2102261.
5 Y. Zhang, D. Wang and S. Wang, *Small*, 2021, **18**, 2104339.
6 F. Lyu, M. Cao, A. Mahsud and Q. Zhang, *J. Mater. Chem. A*, 2020, **8**, 15445–15457.
7 M. Li, Z. Zhao, W. Zhang, M. Luo, L. Tao, Y. Sun, Z. Xia, Y. Chao, K. Yin, Q. Zhang, L. Gu, W. Yang, Y. Yu, G. Lu and S. Guo, *Adv. Mater.*, 2021, **33**, 2103762.
8 H.-S. Chen, T. M. Benedetti, J. Lian, S. Cheong, P. B. O'Mara, K. O. Sulaiman, C. H. W. Kelly, R. W. J. Scott, J. J. Gooding and R. D. Tilley, *ACS Catal.*, 2021, **11**, 2235–2243.
9 M. Luo, Y. Sun, X. Zhang, Y. Qin, M. Li, Y. Li, C. Li, Y. Yang, L. Wang, P. Gao, G. Lu and S. Guo, *Adv. Mater.*, 2018, **30**, 1705515.
10 S. Y. Ma, H. H. Li, B. C. Hu, X. Cheng, Q. Q. Fu and S. H. Yu, *J. Am. Chem. Soc.*, 2017, **139**, 5890–5895.
11 J. Zhang, M. Yuan, T. Zhao, W. Wang, H. Huang, K. Cui, Z. Liu, S. Li, Z. Li and G. Zhang, *J. Mater. Chem. A*, 2021, **9**, 20676–20684.
12 Y. Zuo, D. Rao, S. Li, T. Li, G. Zhu, S. Chen, L. Song, Y. Chai and H. Han, *Adv. Mater.*, 2018, **30**, 1704171.
13 J. Li, C. Wang, H. Shang, Y. Wang, H. You, H. Xu and Y. Du, *Chem. Eng. J.*, 2021, **424**, 130319.
14 G. Hu, L. Shang, T. Sheng, Y. Chen and L. Wang, *Adv. Funct. Mater.*, 2020, **30**, 2002281.
15 W. Zhang, Y. Yang, B. Huang, F. Lv, K. Wang, N. Li, M. Luo, Y. Chao, Y. Li, Y. Sun, Z. Xu, Y. Qin, W. Yang, J. Zhou, Y. Du, D. Su and S. Guo, *Adv. Mater.*, 2019, **31**, 1805833.
16 W. Liang, Y. Wang, L. Zhao, W. Guo, D. Li, W. Qin, H. Wu, Y. Sun and L. Jiang, *Adv. Mater.*, 2021, **33**, 2100713.
17 N. Wang, Y. Xu, Y. Han, C. Gao and X. Cao, *Nano Energy*, 2015, **17**, 111–119.
18 K. Deng, Y. Xu, D. Yang, X. Qian, Z. Dai, Z. Wang, X. Li, L. Wang and H. Wang, *J. Mater. Chem. A*, 2019, **7**, 9791–9797.
19 H. Ma, Z. Zheng, H. Zhao, C. Shen, H. Chen, H. Li, Z. Cao, Q. Kuang, H. Lin and Z. Xie, *J. Mater. Chem. A*, 2021, **9**, 23444–23450.
20 R. Chang, L. Zheng, C. Wang, D. Yang, G. Zhang and S. Sun, *Appl. Catal., B*, 2017, **211**, 205–211.
21 H. H. Li, S. Zhao, M. Gong, C. H. Cui, D. He, H. W. Liang, L. Wu and S. H. Yu, *Angew. Chem., Int. Ed.*, 2013, **52**, 7472–7476.
22 Y. X. Xiao, J. Ying, G. Tian, X. Yang, Y. X. Zhang, J. B. Chen, Y. Wang, M. D. Symes, K. I. Ozoemena, J. Wu and X. Y. Yang, *Nano Lett.*, 2021, **21**, 7870–7878.
23 Y. Ouyang, H. Cao, H. Wu, D. Wu, F. Wang, X. Fan, W. Yuan, M. He, L. Y. Zhang and C. M. Li, *Appl. Catal., B*, 2020, **265**, 118606.
24 L. Huang, J. Zou, J. Y. Ye, Z. Y. Zhou, Z. Lin, X. Kang, P. K. Jain and S. Chen, *Angew. Chem., Int. Ed.*, 2019, **58**, 8794–8798.
25 J. Li, S. Z. Jilani, H. Lin, X. Liu, K. Wei, Y. Jia, P. Zhang, M. Chi, Y. J. Tong, Z. Xi and S. Sun, *Angew. Chem., Int. Ed.*, 2019, **58**, 11527–11533.
26 C. Li, X. Chen, L. Zhang, S. Yan, A. Sharma, B. Zhao, A. Kumbhar, G. Zhou and J. Fang, *Angew. Chem., Int. Ed.*, 2021, **60**, 7675–7680.
27 F. X. Wu, L. Zhang, J. P. Lai, R. Luque, W. X. Niu and G. B. Xu, *Nano Today*, 2019, **29**, 100802.
28 X. D. Yang, J. Xue and L. G. Feng, *Chem. Commun.*, 2019, **55**, 11247–11250.
29 L. Zhang, L. T. Roling, X. Wang, M. Vara, M. Chi, J. Liu, S.-I. Choi, J. Park, J. A. Herron, Z. Xie, M. Mavrikakis and Y. Xia, *Science*, 2015, **349**, 412–416.
30 D. S. He, D. He, J. Wang, Y. Lin, P. Yin, X. Hong, Y. Wu and Y. Li, *J. Am. Chem. Soc.*, 2016, **138**, 1494–1497.
31 X. Bai, J. Geng, S. Zhao, H. Li and F. Li, *ACS Appl. Mater. Interfaces*, 2020, **12**, 23046–23050.
32 Z. Cao, H. Li, C. Zhan, J. Zhang, W. Wang, B. Xu, F. Lu, Y. Jiang, Z. Xie and L. Zheng, *Nanoscale*, 2018, **10**, 5072–5077.
33 W. C. Geng, Y. J. Zhang, L. Yu, J. J. Li, J. L. Sang and Y. J. Li, *Small*, 2021, **17**, 2101499.
34 F. L. Zhao, L. R. Zheng, Q. Yuan, X. T. Yang, Q. H. Zhang, H. Xu, Y. L. Guo, S. Yang, Z. Y. Zhou, L. Gu and X. Wang, *Adv. Mater.*, 2021, **33**, 2103383.
35 L. An, H. J. Yan, B. Li, J. Ma, H. Wei and D. G. Xia, *Nano Energy*, 2015, **15**, 24–32.
36 Z. Wang, H. Zhang, S. Yin, S. Liu, Z. Dai, Y. Xu, X. Li, L. Wang and H. Wang, *Sustainable Energy Fuels*, 2020, **4**, 2950–2955.
37 W. Niu, Z.-Y. Li, L. Shi, X. Liu, H. Li, S. Han, J. Chen and G. Xu, *Cryst. Growth Des.*, 2008, **8**, 4440–4444.
38 F. Zhao, L. Zheng, Q. Yuan, X. Yang, Q. Zhang, H. Xu, Y. Guo, S. Yang, Z. Zhou, L. Gu and X. Wang, *Adv. Mater.*, 2021, **33**, 2103383.
39 G. Kresse and J. Furthmuller, *Comput. Mater. Sci.*, 1996, **6**, 15–50.

40 G. Kresse and J. Furthmuller, *Phys. Rev. B: Condens. Matter Mater. Phys.*, 1996, **54**, 11169–11186.
41 J. P. Perdew, K. Burke and M. Ernzerhof, *Phys. Rev. Lett.*, 1996, **77**, 3865–3868.
42 G. Kresse and D. Joubert, *Phys. Rev. B: Condens. Matter Mater. Phys.*, 1999, **59**, 1758–1775.
43 P. E. Blochl, *Phys. Rev. B: Condens. Matter Mater. Phys.*, 1994, **50**, 17953–17979.
44 J. Yang, R. Hübner, J. Zhang, H. Wan, Y. Zheng, H. Wang, H. Qi, L. He, Y. Li, A. A. Dubale, Y. Sun, Y. Liu, D. Peng, Y. Meng, Z. Zheng, J. Rossmeisl and W. Liu, *Angew. Chem., Int. Ed.*, 2021, **60**, 9590–9597.
45 L. Zhang, W. Niu and G. Xu, *Nanoscale*, 2011, **3**, 678–682.
46 B. Zhang, W. Hou, X. Ye, S. Fu and Y. Xie, *Adv. Funct. Mater.*, 2007, **17**, 486–492.
47 J. Chen, M. Qin, S. Ma, R. Fan, X. Zheng, S. Mao, C. Chen and Y. Wang, *Appl. Catal., B*, 2021, **299**, 120640.
48 Y. Hao, Y. Yang, L. Hong, J. Yuan, L. Niu and Y. Gui, *ACS Appl. Mater. Interfaces*, 2014, **6**, 21986–21994.
49 C. Shang, Y. Guo and E. Wang, *Nano Res.*, 2018, **11**, 4348–4355.
50 L. Wang and Y. Yamauchi, *J. Am. Chem. Soc.*, 2013, **135**, 16762–16765.
51 L. Huang, X. Zhang, Q. Wang, Y. Han, Y. Fang and S. Dong, *J. Am. Chem. Soc.*, 2018, **140**, 1142–1147.
52 W. Yao, X. Jiang, M. Li, Y. Li, Y. Liu, X. Zhan, G. Fu and Y. Tang, *Appl. Catal., B*, 2021, **282**, 119595.